Corrigendum: All planetesimals born near the Kuiper belt formed as binaries

Wesley C. Fraser, Michele T. Bannister, Rosemary E. Pike, Michael Marsset, Megan E. Schwamb, J. J. Kavelaars, Pedro Lacerda, David Nesvorný, Kathryn Volk, Audrey Delsanti, Susan Benecchi, Matthew J. Lehner, Keith Noll, Brett Gladman, Jean-Marc Petit, Stephen Gwyn, Ying-Tung Chen, Shiang-Yu Wang, Mike Alexandersen, Todd Burdullis, Scott Sheppard & Chad Trujillo

In the version of the Supplementary Information originally published the 2001 XR254 measurement was mistakenly omitted from the Binary Objects section in Supplementary Table 1.

All planetesimals born near the Kuiper belt formed as binaries

Supplementary Table 1: Cold Classical KBO Optical Spectral Slopes

Target	s	Target	s
		Single Objects	
15760 - 1992 QB1	23.8 ± 2.3	2000 FS53	33.9 ± 2.0
16684 - 1994 JQ1	35.8 ± 3.0	2000 OH67	24.5 ± 5.1
19255 - 1994 VK8	26.1 ± 3.1	138537 - 2000 OK67	19.0 ± 1.9
1995 DC2	45.5 ± 1.4	2000 QC226	51.3 ± 5.6
1995 WY2	24.3 ± 6.0	2001 HZ58	22.8 ± 5.4
1996 TK66	26.7 ± 3.9	88268 - 2001 KK76	27.1 ± 3.6
1997 CT29	38.1 ± 5.1	2001 OQ108	30.3 ± 4.4
33001 - 1997 CU29	33.8 ± 2.1	2001 QE298	33.6 ± 2.3
52747 - 1998 HM151	27.9 ± 6.0	2001 QO297	32.2 ± 3.7
85627 - 1998 HP151	26.5 ± 6.3	2001 QP297	27.6 ± 1.2
385194 - 1998 KG62	31.7 ± 3.6	2001 QR297	24.5 ± 4.0
85633 - 1998 KR65	30.7 ± 1.5	2001 QS322	22.9 ± 3.3
1998 KS65	27.2 ± 2.4	2001 QX297	24.5 ± 3.5
69987 - 1998 WA25	17.1 ± 6.0	126719 - 2002 CC249	20.8 ± 4.6
1998 WX24	35.5 ± 4.3	2002 CU154	24.5 ± 4.0
1998 WY24	26.2 ± 2.6	2002 PD155	17.8 ± 5.6
1999 HG12	26.4 ± 1.7	2002 PV170	23.7 ± 2.2
1999 HS11	32.8 ± 3.3	385437 - 2003 GH55	24.5 ± 1.8
1999 HV11	24.3 ± 2.3	385447 - 2003 QF113	25.3 ± 3.4
385199 - 1999 OE4	14.6 ± 5.0	2003 QY111	17.3 ± 5.6
66452 - 1999 OF4	30.6 ± 6.0	2006 HW122	17.1 ± 6.1
455171 - 1999 OM4	21.5 ± 3.3	2006 QF181*	26.4 ± 1.2
1999 RC215	39.5 ± 5.3	2013 SP99*	34.7 ± 0.6
137294 - 1999 RE215	36.3 ± 2.5	2013 UL15*	26.1 ± 1.8
1999 RX214	20.9 ± 1.0	2013 UM15*	32.7 ± 1.8
2000 CE105	28.6 ± 4.3	2013 UN15*	36.6 ± 2.4
60454 - 2000 CH105	26.8 ± 1.2	2013 UO15*	27.0 ± 1.2
2000 CL104	21.4 ± 2.4	2013 UP15*	27.2 ± 0.6
2000 CN105	31.4 ± 3.8	2014 UE225*	35.6 ± 0.6
		Binary Objects	
58534 - 1997 CQ29	18.6 ± 5.0	148780 - 2001 UQ18	32.0 ± 4.1
79360 - 1997 CS29	29.7 ± 1.5	2002 VD131	6.8 ± 3.6
1999 RT214	37.4 ± 4.4	2002 VT130	22.7 ± 1.6
66652 - 1999 RZ253	37.1 ± 4.7	2003 HG57	10.2 ± 3.4
2000 CF105	21.6 ± 6.8	2003 QY90	30.6 ± 3.1
80806 - 2000 CM105	33.8 ± 7.0	2003 TJ58	25.0 ± 2.2
2000 CQ114	36.0 ± 0.6	2003 UN284	4.3 ± 5.8
134860 - 2000 OJ67	26.9 ± 3.0	2005 EO304	22.2 ± 3.1
123509 - 2000 WK183	25.4 ± 2.6	2006 BR284	30.8 ± 1.8
2000 WT169	19.9 ± 2.0	2006 CH69	37.3 ± 6.5
88611 - 2001 QT297	25.4 ± 2.3	364171 - 2006 JZ81	32.0 ± 4.2
2001 QW322	-2.2 ± 3.3	2013 SQ99*	33.9 ± 1.8
275809 - 2001 QY297	30.0 ± 2.1	2014 UD225*	14.9 ± 0.6
2001 RZ143	19.2 ± 2.9	2016 BP81*	10.1 ± 1.3
2001 XR254	15.2 ± 4.4		

Note: Objects that are classified as blue have $s < 17\%$. Those objects with non-MPC designations are internal OSSOS designations of cold classical objects. * - colours measured by Col-OSSOS.

Supplementary Table 2: Observed Binary Properties

Target	Separation (",km)	Secondary:Primary Brightness Ratio
2002 VD131	$0.48 \pm 0.02, 14900 \pm 600$	$0.061^{+0.012}_{-0.004}$
2016 BP81	$0.369^{+0.02}_{-0.01}, 11300^{+600}_{-300}$	$0.81^{+0.09}_{-0.06}$
2013 SQ99	$0.39^{+0.02}_{-0.01}, 13300^{+700}_{-300}$	$0.65^{+0.06}_{-0.05}$
2014 UD225	$0.67 \pm 0.02, 21400 \pm 600$	0.12 ± 0.01

Note: Uncertainties are $1 - \sigma$ uncertainties. The confidence intervals have been combined using all images available for each target for the quoted uncertainties. Binary properties were measured from Gemini-GMOS images of 2013 SQ99 and 04h45. For 2016 BP81, only the single GMOS frame with the best image quality was used as it was the only frame to resolve the two components. The single images with best image quality from each of the Magellan and CFHT image sequences were used to measure the properties of 2002 VD131.

Supplementary Table 3: Initial and final properties of example cloud collapse simulations

| Ω (Ω_{circ})	r_p (km)	r_s (km)	a_{bin} (km)
0.1	138.5	66.8	4731
0.5	99.2	69.9	5281
0.75	90.2	65.9	7066

Note: Initial mass M_{tot} and cloud angular velocity are presented. $\Omega_{circ} = \sqrt{\frac{GM_{tot}}{R^3_{tot}}}$ where R_{tot} is the initial cloud radius. Final primary and secondary radii and binary semi-major axis at end of the simulations are also presented.
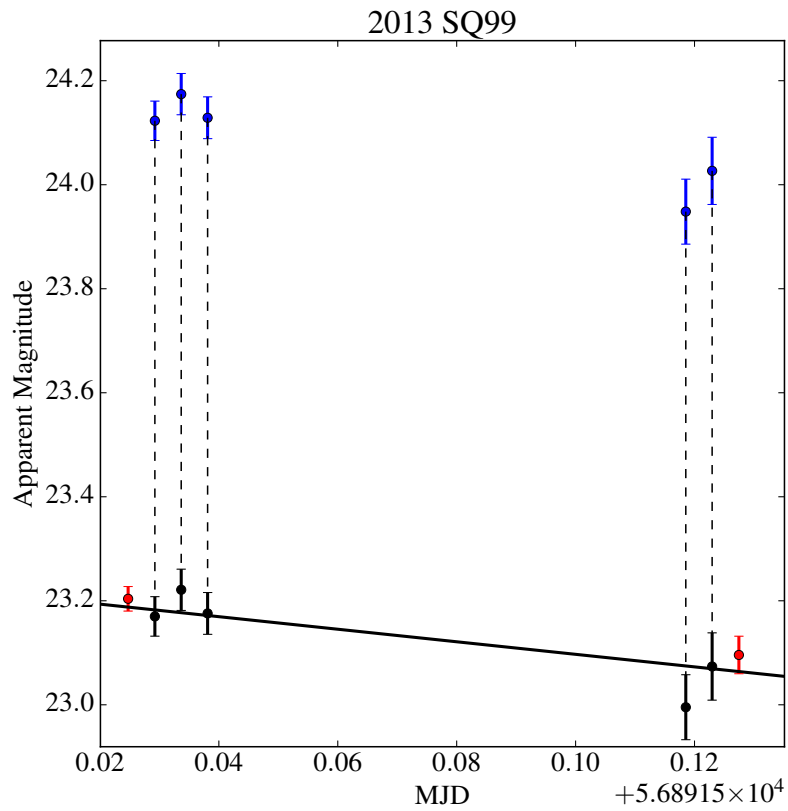
Supplementary Figure 1: Observed apparent magnitudes of binary 2013 SQ99 in the r' (red) and g' (blue) filters. Black points show r' magnitudes estimated from the g' observations and the mean (g'-r')= 0.89 ± 0.02 colour in the Gemini filters. The best-fit linear lightcurve which decreases ∼ 0.04 mags from start to end of sequence is shown by the solid black line.
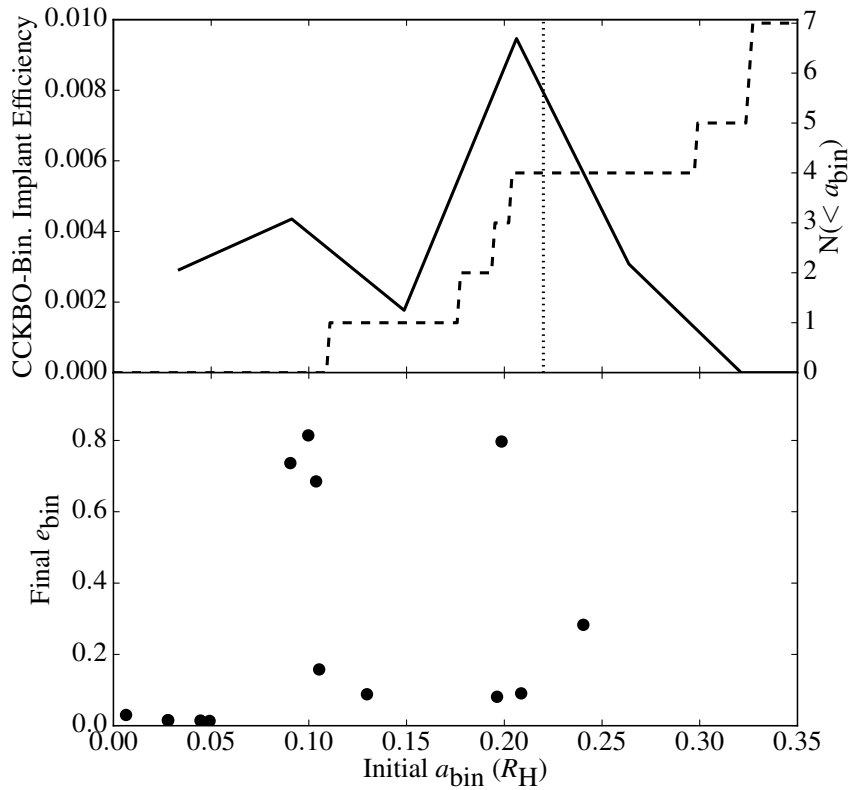
Supplementary Figure 2: Top: the solid line presents the efficiency of implantation by migration of binaries into the cold classical region as a function of initial binary semi-major axis. The dashed line presents the cumulative distribution of singles implanted in the cold classical region as a function of initial binary semi-major axis. The vertical dashed line presents the current binary semi-major axis of the widest separated known, cold classical binary, 2001 QW322. Bottom: final eccentricity of CCKBO binary survivors vs. initial binary semi-major axis.
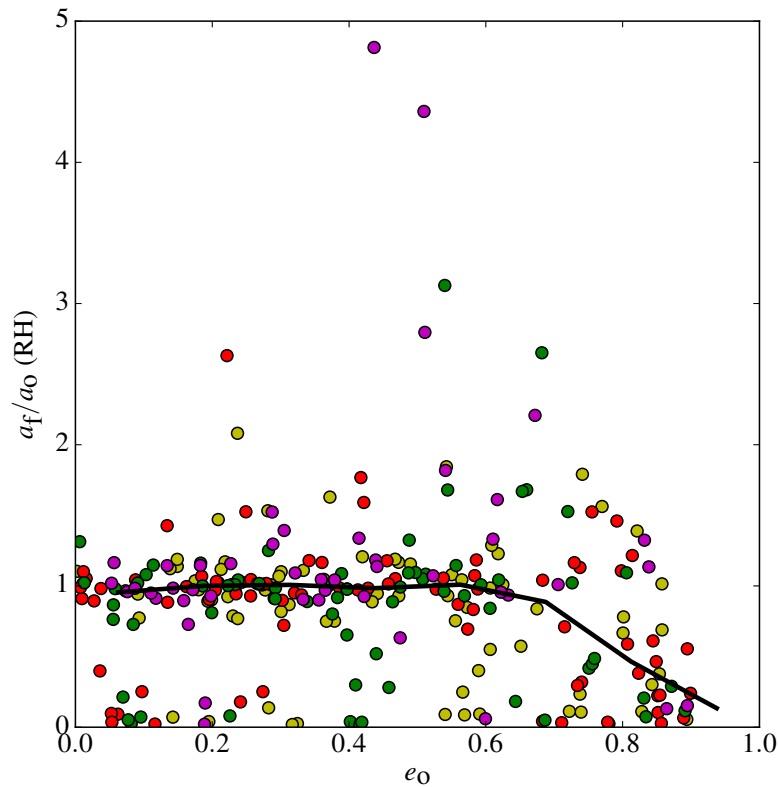
Supplementary Figure 3: Ratio of final and initial binary semi-major axis vs. initial binary eccentricity for the binary evolution simulations of Bruini and Zanardi (2016) which assumed a tidal quality factor of Q=10. Yellow, red, green, and magenta points correspond to binary size ratios of 0.25, 0.5, 0.75, and 1. The black line depicts the mean ratio as a function of initial eccentricity for the entire sample. A mean reduction in semi-major axis is observed for eccentricities $e_o \gtrsim 0.6$ where tidal forces become the dominant driver of the binary evolution.
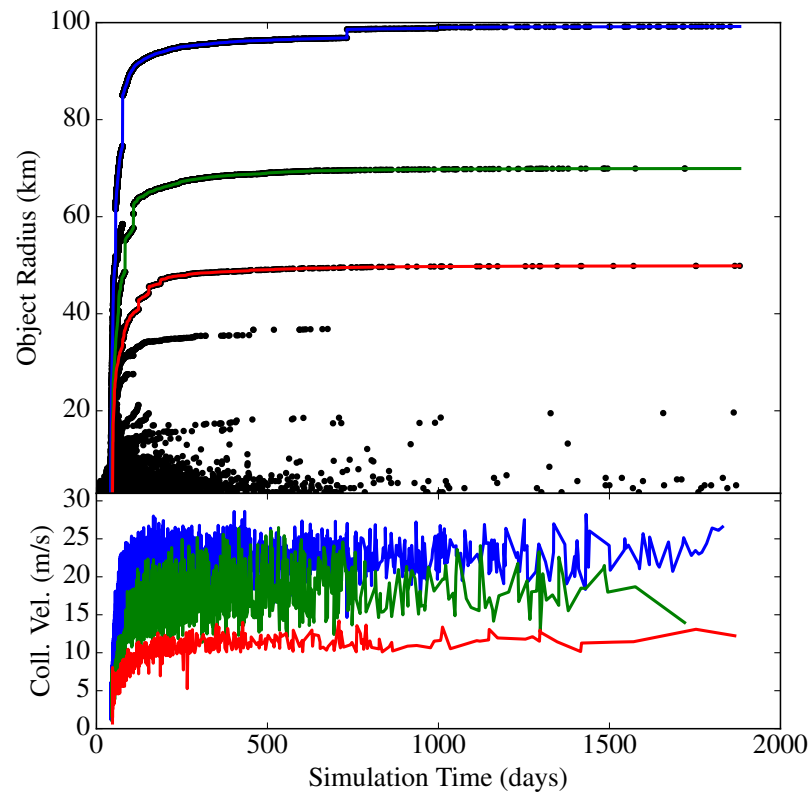
Supplementary Figure 4: The collisional growth during the collapse of a grav- itationally bound cloud. The growth and collisions experienced by the largest three bodies which the simulation produces are traced by the blue, green, and red lines, respectively. The top panel displays the evolution of the radius of each object as a function of time. Black dots denote when a collision occurs, and the radius of the merged body. The bottom panel displays the collision velocities of each collision in the top panel. The collision velocities are very similar regard- less of impactor size. As exhibited by the nearly smoothly increasing radius of the large bodies with time, impacts are dominated by the smallest bodies in the simulation.